



OPEN ACCESS

EDITED BY

Hebe Cremades,
University of Mendoza and Conicet, Argentina

REVIEWED BY

Ritesh Patel,
Southwest Research Institute Boulder,
United States

Scott William McIntosh,
National Center for Atmospheric Research
(UCAR), United States

*CORRESPONDENCE

Zou Peng,
✉ awaken@hit.edu.cn

RECEIVED 12 January 2024

ACCEPTED 24 July 2024

PUBLISHED 28 August 2024

CITATION

Zou P, Jiang C, Bian X and Wang J (2024)
Triggering mechanism of an eruptive filament
located in a weak active region.
Front. Astron. Space Sci. 11:1369362.
doi: 10.3389/fspas.2024.1369362

COPYRIGHT

© 2024 Zou, Jiang, Bian and Wang. This is an open-access article distributed under the terms of the [Creative Commons Attribution License \(CC BY\)](https://creativecommons.org/licenses/by/4.0/). The use, distribution or reproduction in other forums is permitted, provided the original author(s) and the copyright owner(s) are credited and that the original publication in this journal is cited, in accordance with accepted academic practice. No use, distribution or reproduction is permitted which does not comply with these terms.

Triggering mechanism of an eruptive filament located in a weak active region

Peng Zou^{1*}, Chaowei Jiang¹, Xinkai Bian² and Juntao Wang^{2,3}

¹Shenzhen Key Laboratory of Numerical Prediction for Space Storm, Institute of Space Science and Applied Technology, Harbin Institute of Technology, Shenzhen, China, ²Institute of Space Science and Applied Technology, Harbin Institute of Technology, Shenzhen, China, ³School of Physical Science and Technology, Lingnan Normal University, Zhanjiang, China

Introduction: The triggering mechanism for filaments located in a weak magnetic field typically leans toward magnetohydrodynamic instabilities due to the weak magnetic strength inherent in filament structures. However, a subset of eruption events associated with significant flares remains. Therefore, we seek to understand the role that reconnection plays in the eruption of filaments with weak magnetic fields.

Methods: We reconstruct the coronal magnetic field of an eruptive filament located in a relatively weaker magnetic environment, and analyze the magnetic field properties such as twist number and squashing factor.

Results: This filament remains stable until the expansion of the heated bright arcades underneath. This expansion initially activates the filament, prompting its upward movement, leading to a gentle reconnection slightly to its south. The ensuing reconnection continues to propel the filament upward with uniform acceleration. These upward motions cause the drainage of filament mass, likely activating the torus instability of the filament. This torus instability then triggers the final eruption of the filament, successfully generating a coronal mass ejection (CME) and leaving behind a double-ribbon flare.

Discussion: We conclude that the torus instability serves as the primary triggering mechanism of this eruption, while pre-eruption reconnection plays a role in pushing the filament upward to meet the instability condition.

KEYWORDS

Sun: coronal mass ejections (CMEs), Sun: filaments, prominences, Sun: magnetic fields, magnetic reconnection, magnetic reconstruction

1 Introduction

The triggering mechanisms of coronal mass ejections (CMEs) have been extensively investigated over several decades (Sakurai, 1976; van Ballegoijen and Martens, 1989; Antiochos et al., 1999; Chen and Shibata, 2000; Moore et al., 2001; Aulanier et al., 2010; Török and Kliem, 2005; Kliem and Török, 2006; Jiang et al., 2021). The CSHKP model, a tool to interpret observations, was developed through several studies (Carmichael, 1964; Sturrock, 1966; Hirayama, 1974; Kopp and Pneuman, 1976). This model describes that a magnetic flux rope (MFR) is activated in some manner, triggering an eruption. The MFR is ejected and becomes the CME, while the newly reconnected arcades underneath form the flare loops. Various mechanisms have been proposed to elucidate

this triggering mechanism and explain why the evolution of the coronal magnetic field can lead to such massive eruptions. Some of these mechanisms effectively interpret observed eruption phenomena and the associated magnetic configurations, with numerical simulations providing supporting evidence for their efficacy in initiating eruptions. These mechanisms can be broadly categorized into two types: one dominated by magnetic reconnection and the other by the ideal magnetohydrodynamics (MHD) instability domain.

In the first type, the process of reconnection plays a key role in transforming magnetic energy into kinetic energy. Magnetic arcades undergo shearing near the polarity inversion line (PIL), accumulating substantial free magnetic energy. Subsequently, converging flows compel these arcades to reconnect with adjacent ones, forming a new magnetic flux rope (MFR). This MFR is then propelled into the higher corona, potentially leading to the generation of a CME. This mechanism is known as the tether-cutting model (Moore et al., 2001), where reconnection beneath the MFRs generates an upward force that sustains the propagation of MFRs. Reconnection can also occur above the MFRs, triggering CMEs as described by the breakout model (Antiochos et al., 1999). In this model, a continually sheared arcade underneath a quadrupole field pushes the null point of the quadrupole field, leading to reconnection. The reconnection weakens the constraining force of the sheared core field, allowing it to escape from the corona and become a CME.

However, some studies argue that magnetic reconnection alone is unlikely to be able to generate a CME (Aulanier et al., 2010; Zou et al., 2019a). MFRs may eject themselves through MHD instabilities, such as kink instability. This instability transforms the twist of the MFR into writhe, causing the axis of the MFR to rise and trigger further eruption when the twist is sufficiently high (Sakurai, 1976; Török et al., 2004). As the rising MFR crosses a height where the background field strength rapidly decreases, it breaks the constraint of the background field, leading to the generation of a CME. The theoretically critical rate of decrease in the background magnetic field strength, denoted as n , is approximately 1.5 (Török and Kliem, 2005; Kliem and Török, 2006; Aulanier et al., 2010). This phenomenon is referred to as torus instability.

In addition to these models, other factors influence the eruption of magnetic flux ropes (MFRs) or filaments. For example, the drainage of filament mass may disrupt the equilibrium of the filament structure (Fan, 2018; Jenkins et al., 2019), and inflows from the higher corona can disturb and even destabilize low-coronal structures when they approach the solar surface (Seaton et al., 2021).

Typically, these processes mainly unfold within active regions, where the core magnetic field possesses sufficient strength to overcome the constraining field, yielding ample free energy to sustain further propagation (Yashiro et al., 2005; Cheng et al., 2010; Jing et al., 2014; Duan et al., 2021). However, observations indicate that CMEs can originate not only from active regions but also from areas with weak magnetic fields (McCauley et al., 2015; Zou et al., 2019b). Additionally, a statistical examination of filament eruptions reveals that more eruptions occur in relatively quiescent areas, with approximately half ultimately evolving into CMEs (McCauley et al., 2015).

These eruptions exhibit different triggering mechanisms (Zou et al., 2019b). In the case of active region filaments, both

instability and reconnection can serve as triggers for CMEs, with their probabilities being relatively similar. Conversely, magnetic reconnection appears to play a minor role for quiescent filaments. This is plausible, considering that the magnetic field in the quiescent sun is comparatively weaker than in active regions. It is noteworthy that quiescent flares can also produce flares higher than C-class, as exemplified by the well-known filament eruption on 31 August 2012. These occurrences are also documented in the statistical studies conducted by McCauley et al. (2015) and Zou et al. (2019b). The reduced magnetic field strength implies a weaker tension force generated by reconnection to propel the magnetic configuration. Consequently, reconnection tends to be less significant in the initiation of quiescent filament ejections, often occurring significantly later than the onset of the high-speed eruption phase (Zou et al., 2019b). This is supported by observations that flare onset lags obviously behind the filament acceleration.

However, some filament eruptions in the quiescent sun exhibit onset times very close to the flare starting time, aligning with the reconnection onset time (Zou et al., 2019b). For these events, it is challenging to unambiguously determine whether the trigger mechanism involves a reconnection process or a non-reconnection process. Nevertheless, reconnection evidently plays a considerable role in these eruptions, as indicated by previous studies; it is capable of initiating ejections, facilitating further propagation, and even interrupting eruptions (Moore et al., 2001; Antiochos et al., 1999; Jiang et al., 2021; Peng et al., 2022). The precise trigger mechanisms and the role of magnetic reconnection in filament eruptions located in relatively weaker magnetic fields, such as quiescent filaments and parts of intermediate filaments, remain an intriguing subject of investigation.

Due to challenges in reconstructing the coronal magnetic field in the quiescent sun, previous studies have faced difficulties in quantifying magnetic field characteristics, leading to ambiguity in diagnosing trigger mechanisms. In this study, we address this issue by employing an MHD relaxation model called the CESE-MHD-NLFFF code to extrapolate the magnetic configuration of an eruptive filament (Jiang and Feng, 2013). This model has been previously utilized for reconstructing several filaments within a weak magnetic environment, both quiescent filament and intermediate filament, demonstrating a close fit between the extrapolated configuration and the observed filament spine (Jiang et al., 2014; Peng et al., 2022). In this article, we performed an analysis of the eruption of a filament located in a weak active region. With the help of the extrapolated configuration, our investigation aims to unravel the eruptive mechanism of this filament, specifically exploring the role of magnetic reconnection in the eruption scenario.

The article is organized into the following sections. In Section 2, we present the data set and methods. Section 3 summarizes the evolution of the filament eruption and the related magnetic characteristics. Section 4 introduces a scenario to describe the eruption and discusses the role of reconnection in this event.

2 Data and method

The filament is situated in between active regions NOAA AR11480 and NOAA 11477, in a zone that, although not cataloged by NOAA as active, can be considered as a weak active region. It

initiated its eruption around 23:00 UT and completed the eruption by approximately 23:40 UT on 11 May 2012. The Atmospheric Imaging Assembly (AIA) (Lemen et al., 2012) onboard the Solar Dynamics Observatory (SDO) effectively recorded this filament eruption in EUV filters. SDO/AIA has seven EUV filters, offering a pixel size of 0.6 arcsec per pixel and a cadence of 12 s.

To study the distribution of magnetic features and photosphere velocity and reconstruct the coronal magnetic field, we employed the magnetograms of the Helioseismic and Magnetic Imager (HMI) (Scherrer et al., 2012; Schou et al., 2012), also onboard the SDO. These magnetograms have a pixel size of 0.5 arcsec per pixel and a cadence of 45 s for line-of-sight (LOS) magnetograms, with a cadence of 720 s for vector magnetograms. The fact that the SDO team has produced Space-weather HMI Active Region Patch (SHARP) (Bobra et al., 2014) data for the region (HMI SHARP 1642) further supports our appreciation of this region as active. However, the SHARP area covers only the northern part of the filament and, therefore, cannot be used for our study. To encompass the entire filament structure, we utilized the full-disc vector magnetogram. Despite its difference from SHARPs, the HMI group provides programs to resolve the 180° ambiguity and correct the projection effects using the methodologies proposed by Metcalf (1994) and Gary and Hagyard (1990).

It is noteworthy that the study area is within a weak active region for which many non-linear force-free field (NLFFF) codes fail to extrapolate the coronal field due to data uncertainties of the weak field. The CESE-MHD-NLFFF code appears to be the only method we have mastered that can reconstruct a coronal field in reasonable consistency with the observations in such weak field regions, as has been demonstrated in studies of a few events (Jiang et al., 2014; 2019; Duan et al., 2022; Peng et al., 2022). Hence, we employed the CESE-MHD-NLFFF extrapolation method to reconstruct the coronal magnetic field.

Using the reconstructed magnetic configuration, we calculated several parameters to quantify magnetic field characteristics. These parameters include the twist number and squashing factor of magnetic tubes, as well as the decay index of the background magnetic field overlying the filament. The twist number T_w quantifies the turns of a magnetic field line winding around its close field lines. It is calculated using the formula:

$$T_w = \int_L \frac{(\nabla \times \vec{B}) \cdot \vec{B}}{4\pi B^2} dl \quad (1)$$

where L is the length of magnetic field line, and \vec{B} is the magnetic flux density. The decay index $n = -\partial(\log B)/\partial(\log h)$ measures the degree of decay of the potential field strength overlying the core magnetic configuration. Theoretically, a decay index $n = 1.5$ is considered a critical value for triggering torus instability (TI) (Filippov and Den, 2000; Aulanier et al., 2010). The squashing factor Q (Titov et al., 2002) quantifies locations where magnetic connections undergo drastic changes (Démoulin, 2006), with a higher Q value indicating regions prone to magnetic reconnection.

3 Results

The SDO/AIA provides coverage of the entire structure and evolution of the observed eruption. This filament initiated its

eruption at approximately 23:05 UT on 11 May 2012, resulting in a double-ribbon flare. Prior to the eruption, several notable phenomena were observed in connection with the filament, such as bright arcades beneath the middle section of the filament, seemingly rooted in the strongest magnetic polarities (see Figure 1, panels A and D). In addition, material draining from the filament spine was frequently observed in both footpoints (see Figure 2). The yellow slice indicates the drainage flow from the spine to the north footpoint of the filament, while the cyan slice indicates the drainage flow from the spine to the south footpoint.

To illustrate the complete trajectory of the eruption process, we selected a slice tracing the eruption direction to construct a time-distance map (depicted in Figure 3). Additionally, as we observed flare ribbons adjacent to the filament, we incorporated the soft X-ray (SXR) flux onto the map using a solid white line (Chamberlin et al., 2009). Notably, several fluctuations in the SXR flux were discernible. We endeavored to ascertain if these fluctuations corresponded to specific events and noted that the bright arcades beneath the filament were luminous during this period. Consequently, we delineated a box to compute the light curve, represented by a solid red line on the map. Upon comparison of these two lines, we observed that the light curve increase was almost synchronous with the SXR flux jump around 22:30 UT.

Furthermore, we estimated the approximate transverse velocities of the filament using the trajectory depicted in the time-distance map (shown in Figure 4). They are the derivation of each distance over time (using the central deference). Based on this velocity, we roughly divided the eruption process into four phases. The first is the stable phase, during which the filament remained nearly stable with minimal upward velocity. These velocities were likely caused by material oscillations. The next phase, the slow upraise phase, exhibited a very slight velocity, approximately 1 or 2 km s⁻¹, starting around 22:28 UT and lasting over 20 min. We believe this phase marked the beginning of the entire eruption process. Following this, the uniform acceleration phase occurred from 22:52 UT to 23:09 UT, characterized by the filament undergoing uniform acceleration, depicted by a straight dashed red line in Figure 4. The final phase, the eruption phase, featured exponential acceleration from 23:09 UT until the filament exited our selected field of view. Throughout the slow upraise and uniform acceleration phases, drainage flows were detectable at both filament footpoints. Towards the end of the uniform acceleration phase, although the light curve decreased, the velocity accelerated impulsively. This unstoppable acceleration culminated in the final eruption. Subsequent to this phase, both the SXR flux and the intensity adjacent to the filament increased impulsively, signaling the onset of the flare.

As coronal activities are predominantly governed by the magnetic field, obtaining a comprehensive magnetic configuration of this filament is crucial for understanding the physics underlying its evolution, particularly the eruption event. In Figure 5, we present the magnetic configuration of the filament alongside the observations for comparison. As is well known, the filament materials are supported by twisted or arched magnetic tubes, and when they fill up the tubes, they will manifest as filament fibrils. Thus, the traced magnetic lines are used to represent the filament fibrils. As can be seen, most magnetic field lines (marked in magenta lines) align well with the structure of the filament. Notably, features such as the large hook-like structure

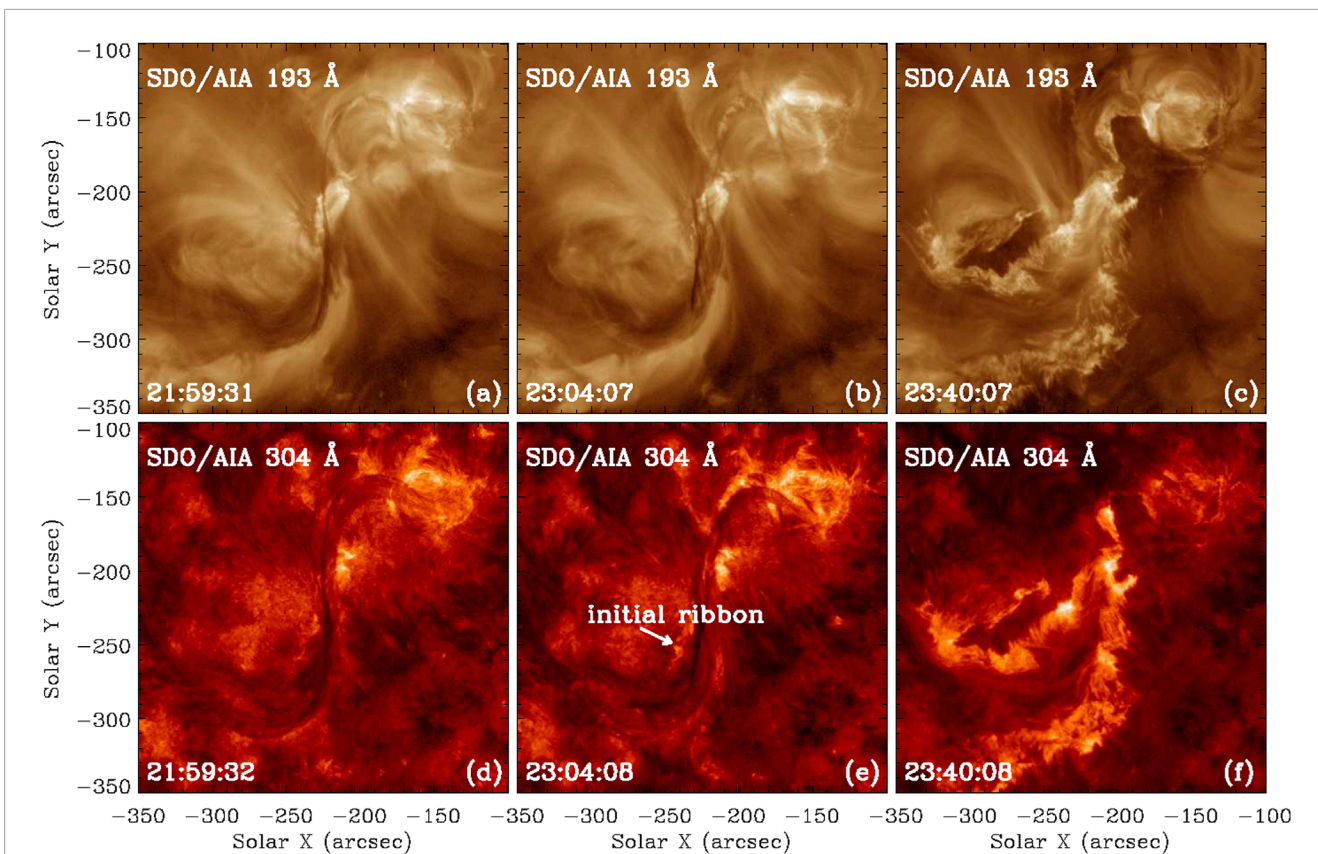


FIGURE 1 Multiple snapshots are presented to depict the progression of the filament in both 193 Å and 304 Å filters. The luminous arcades are clearly observable in panels (A, B). Additionally, the initial flare ribbons are highlighted with an arrow in panel (E).

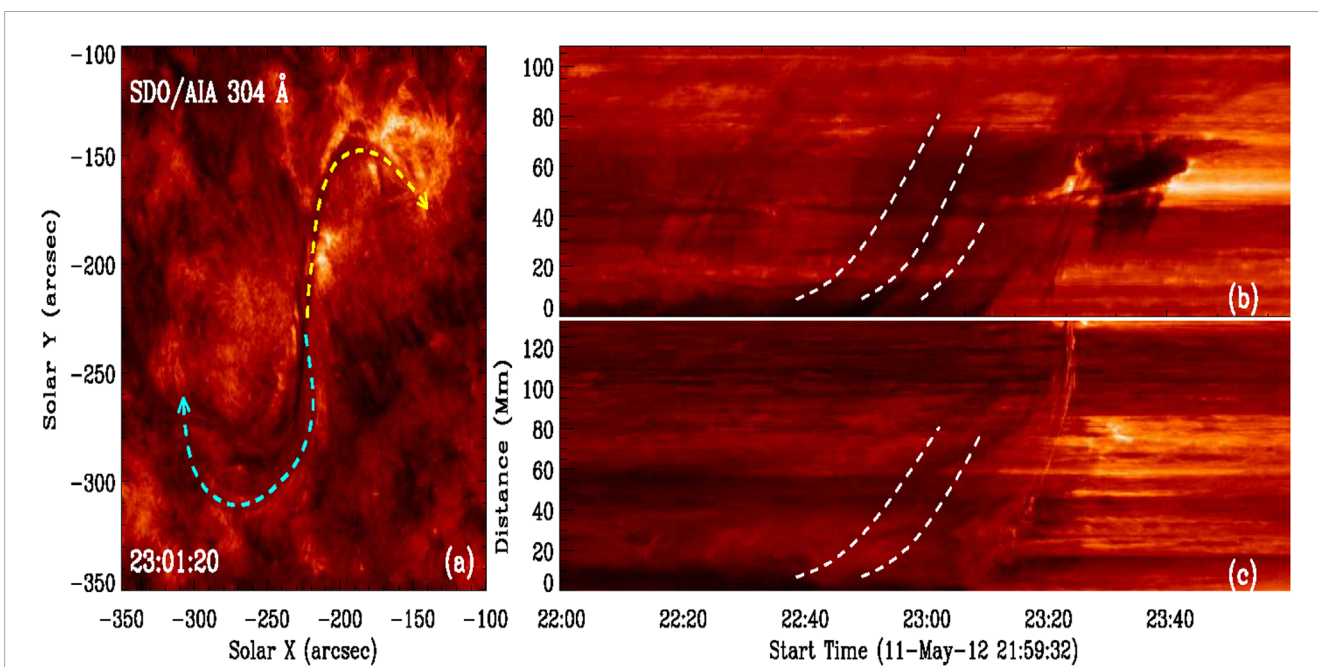
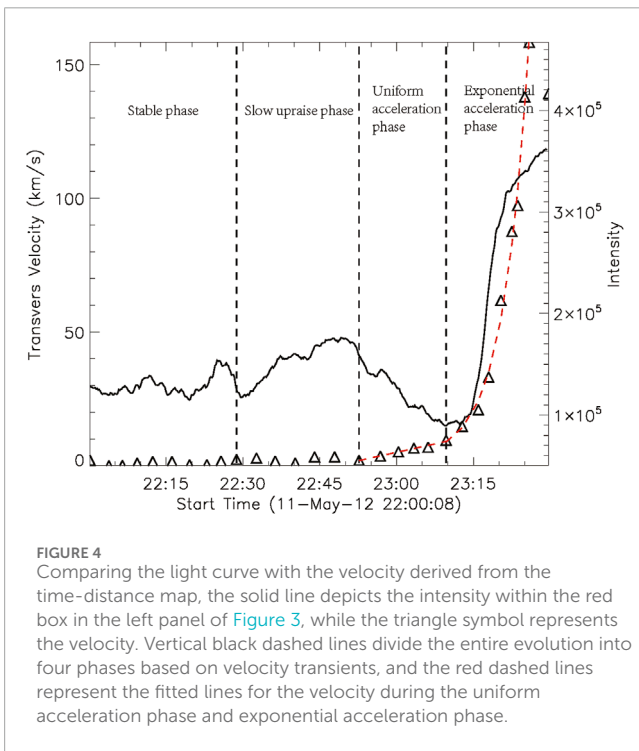
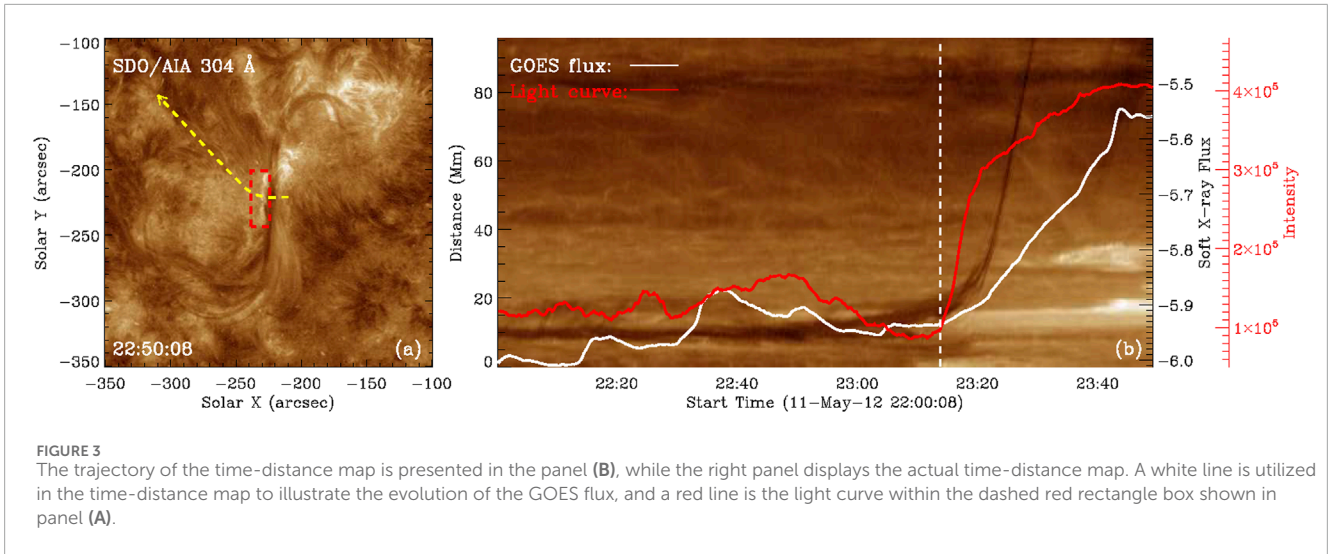


FIGURE 2 The time-distance map along the filament spine illustrates the drainage flows, detectable from approximately 22:37 UT onward. The arrows in panel (A) indicates the direction of the slices. The panel (B) displays the yellow slice, while the panel (C) showcases the cyan slice. The white dashed lines in the two panels on the right represent the flows along the slice, indicating the drainage flow of the filament spine.



with attached threads in the southern part of the filament and the straight spine in the middle are effectively captured by the extrapolated magnetic field lines. Despite some persistent disparities between the observed filament and extrapolated magnetic lines, two notable issues arise. First, the alignment discrepancy between the observed north footpoint and the extrapolated field lines suggests that the observed north filament footpoint originates from magnetic patches situated further westward. Second, the southern half of the filament spine is discernible, yet we encounter difficulty in tracing out a bundle of magnetic lines to replicate it accurately. These discrepancies likely stem from the presence of a weak

magnetic field. It is worth noting that this filament is situated within a weak active region, with filament fibrils rooted in both strong and weak magnetic fields. However, the weak magnetic field exhibits a low signal-to-noise ratio, rendering the extrapolated field from weak magnetic sources unreliable. Consequently, we can only trace out those field lines rooted in the strong magnetic field and endeavor to select lines that closely match the observed fibrils. While we may not entirely replicate the filament structure, the traced magnetic lines still adequately align with the observed filament threads. Consequently, we believe this extrapolation can offer valuable insights into analyzing the triggering mechanism of the eruption.

Based on the observations, the initial detection of the corresponding intensity enhancement occurs south of the red box marked in Figure 3. Additionally, the traced magnetic lines appear to be discontinuous in this area. Therefore, we designate this area as the center, and the magnetic lines associated with the filament can be broadly classified into three bundles. The upper bundle extends from the north footpoint of the filament and roots in the strongest negative magnetic polarities. The middle bundle, which we mark using green lines in Figure 5, roots between the two strongest opposite polarities in the middle, and this bundle relates to the initial flare ribbons. The bottom bundle extends from the strongest positive polarities, forming a large hook-like structure. The previously mentioned bright arcades beneath the filament, marked in yellow in the figure, are well-fitted to the observed arcades. A side-view figure (see Figure 6) illustrates their height relative to the filament spine, revealing that the arcades are slightly below it. Additionally, we have chosen specific filament arcades delineated by green lines to illustrate the magnetic field lines associated with the initial intensity enhancement. These arcades are situated between the middle bundle and the south bundle.

As mentioned in Section 2, certain characteristic parameters indicate whether the magnetic configuration is in an unstable critical state. These parameters include the twist number of the filament spine and the decay index at the height of the filament axis. In Figure 7, we present a twist map of a longitudinal section

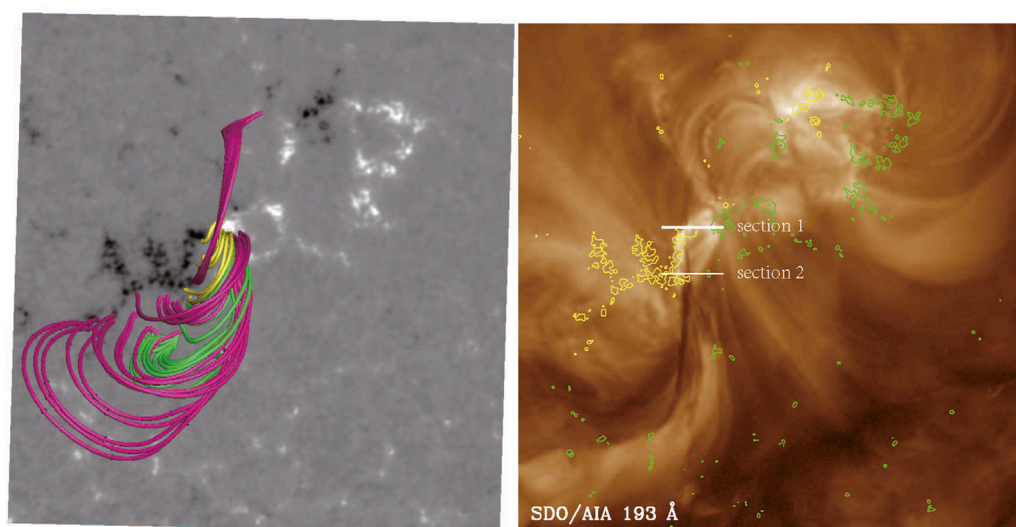


FIGURE 5

Comparison between the extrapolated magnetic field lines with the observed filament in the 193 Å filter: the magenta lines represent the filament arcades, the green lines depict the magnetic field lines associated with the initial flare ribbon, and the yellow lines indicate the bright arcades. The contours represent $\pm 200\text{G}$, with green indicating positive and yellow indicating negative.

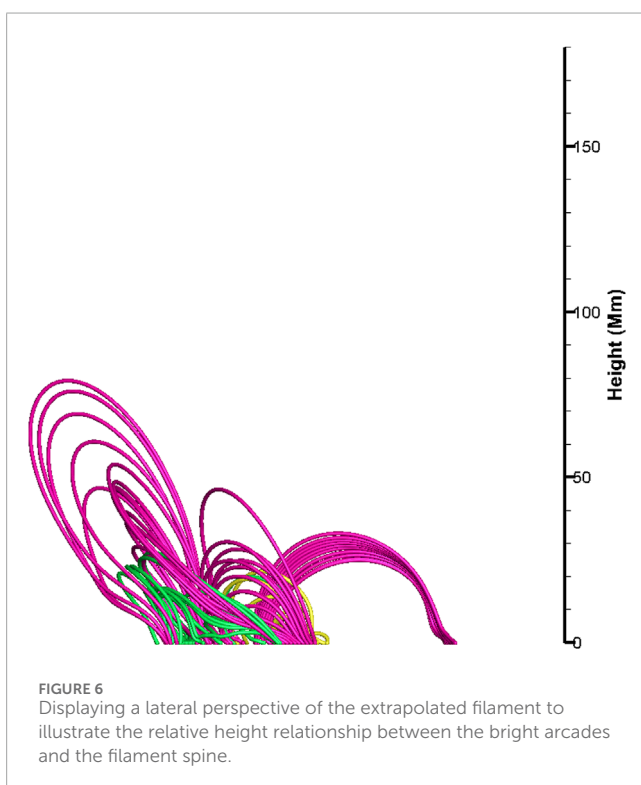


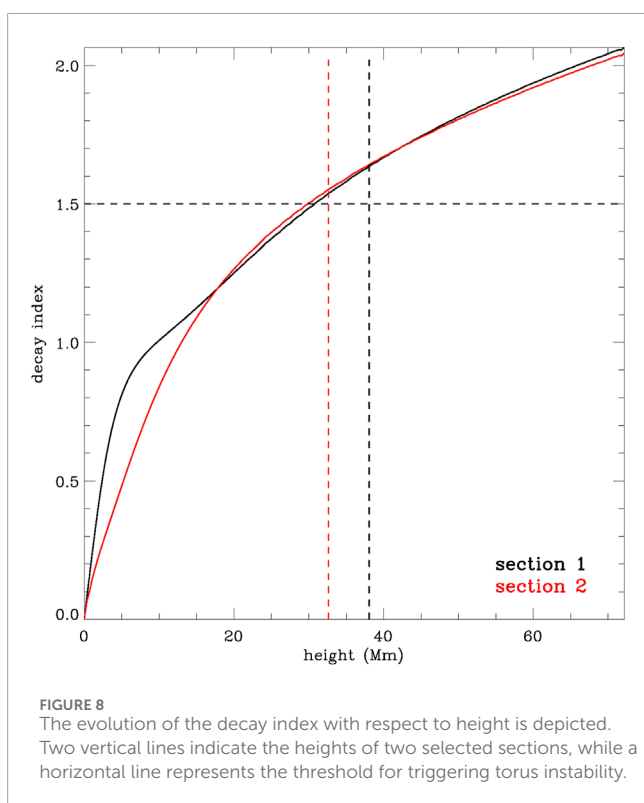
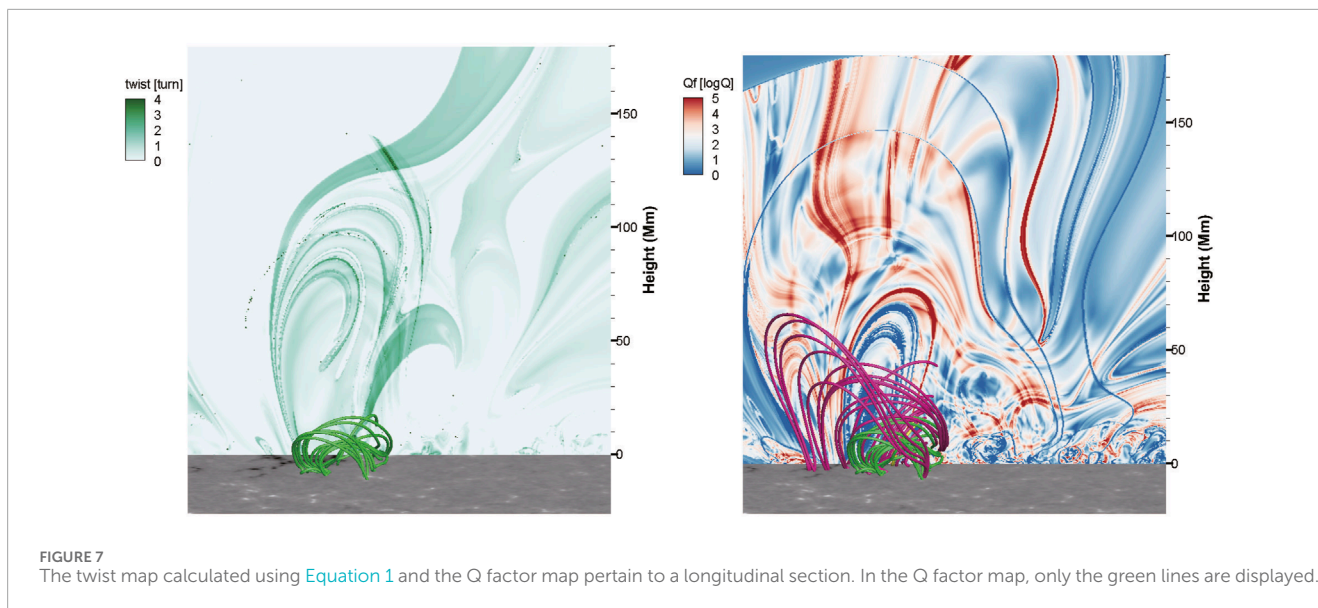
FIGURE 6

Displaying a lateral perspective of the extrapolated filament to illustrate the relative height relationship between the bright arcades and the filament spine.

in the middle part of the filament. The twist is relatively low, with most magnetic field lines of the filament exhibiting nearly one turn. Based on the observed filament, the filament should be a sinistral filament. According to Martin's Rule (Martin et al., 1992) and its supplementary explanation by Chen et al. (2014), a sinistral

filament is typically considered to have inverse polarity when threads exhibit left-bearing orientation, while right-bearing threads indicate normal polarity. In our scenario, the predominant left-bearing orientation suggests that the supporting magnetic structure is likely a magnetic flux rope (MFR). Thus, we hypothesize the existence of an axis within this filament, surrounded by a cluster of tightly twisted magnetic field lines, constituting the MFR. This flux rope likely extends from the north footpoint to the south footpoint of the filament. The magnetic lines traced out represent those enveloping the MFR. However, owing to the low signal-to-noise ratio, tracing magnetic lines from one footpoint to the other often results in accumulated errors, particularly when one footpoint is situated in a weak magnetic area or when magnetic lines are excessively lengthy. This discrepancy likely accounts for our inability to accurately replicate the entire filament spine within the extrapolated magnetic field.

Similarly, in the squashing factor map presented in the next panel with the same location, the Q values are also relatively lower. Nevertheless, all the designated green lines are positioned in the region with a Q factor exceeding 10^2 , indicating their location within the quasi-separatrix layer (QSL). The extrapolated filament arcades have a height of about 35 Mm, which is characteristic of quiescent filaments. Consequently, we computed the decay index along the connection line between the PIL and the filament spine. Figure 8 illustrates the changes in the decay index with height. Two specific sections are selected, and their positions are indicated by two solid white lines in Figure 5. Notably, both heights of the filament spine are higher than the theoretical critical decay index for torus instability, indicating a critical state conducive to torus instability. Also, we calculate the decay index of additional points along the PIL, and we find that the decay indexes are consistently around 1.6. Therefore, we believe that the results presented in Figure 8 are



sufficient to demonstrate that the filament is already under torus instability.

4 Discussion and conclusion

Solar eruptions have been extensively studied from both observational and theoretical perspectives (Sakurai, 1976;

Moore et al., 2001; Török et al., 2004; Török and Kliem, 2005; Aulanier et al., 2010; Jiang et al., 2019; Zou et al., 2019a; Peng et al., 2022). However, there is a notable scarcity of research focusing on the eruptions of solar structures within weak magnetic environments. The challenges in coronal magnetic reconstruction limit our ability to determine the triggers for these eruptive phenomena. Nevertheless, recent statistical research emphasizes the significance of investigating quiescent solar eruptions to gain a comprehensive understanding of solar eruption dynamics (McCauley et al., 2015; Zou et al., 2019b).

Building on previous work utilizing the CESE-MHD-NLFFF model (Jiang et al., 2014; 2019; Duan et al., 2022; Peng et al., 2022), which has demonstrated its effectiveness in reconstructing structures rooted in the network field of weak active areas, we present a case study focusing on a filament located in a weak active region. In this study, we employ the model to reconstruct the complete body of the filament, utilizing extrapolated coronal magnetic field lines. Most of these reconstructed lines align well with the observed filament. We leverage this reconstructed configuration to conduct a detailed analysis of the trigger process leading to the eruption of this filament.

First, as discussed in Section 3, the eruption process is segmented into four phases. The initial phase transition triggers the activation of a nearly stable filament. This occurs several minutes after the intensity enhancement observed in the selected box in Figure 4, primarily induced by the east footpoint of the underlying arcades (refer to the attached movie). Consequently, the arcades experience heating, leading to filament activation. Thus, we posit that arcade heating initiates upward expansion, propelling the filament. This upward motion persists for more than 20 min, during which the arcade intensity peaks. At this peak, intensity enhancement spreads slightly southward from the arcade footpoint (as seen in the left panel of Figure 3). Shortly after this localized heating, the filament undergoes uniform acceleration. Previous studies have associated such parabolic height profiles, indicative of linear velocity profiles,

with reconnection acceleration processes (Lynch et al., 2004). Hence, we infer that the new heating patch signifies magnetic reconnection, likely associated with the green lines delineated in Figure 5. These green lines originate from the bright patch within an area exhibiting relatively high quashing factor values (refer to the Q value map in Figure 7). However, this reconnection is too subtle to elicit corresponding changes in the SXR flux. Approximately 15 min later, the velocity undergoes an impulsive increase, with acceleration rising in tandem with filament height, as noted by Mierla et al. (2013). This velocity increase aligns well with an exponential function, consistent with previous assertions linking such evolution to torus instability or kink instability (Török and Kliem, 2005; Kliem and Török, 2006). Although no kink motions are discernible in the observations, we posit that this phase likely results from torus instability. Subsequently, after the filament attains sufficient height, reconnection propagates throughout, leading to an impulsive increase in SXR flux, indicative of flare formation. Such forced reconnections by filament eruptions are also reported by Srivastava et al. (2021).

This discussion depicts the inferred scenario of the eruption process based on observations. However, several aspects warrant clarification. First, what constitutes the primary triggering mechanism for the ultimate eruption? In our interpretation, both reconnection and instability play pivotal roles in driving the final eruption. In the statistical analysis by Zou et al. (2019b), the authors assert that magnetic reconnection triggers the eruption, as its onset slightly precedes that of the flare. They employ an equation featuring linear and exponential forms to model the eruption trajectory. As their fitting function lacks piecewise characteristics, they set the eruption onset when the gradient (i.e., velocity) reaches twice the initial gradient. Conversely, our detailed analysis reveals a specific time point in the velocity evolution where velocity shifts from linear to impulsive. This transition suggests that reconnection (during the uniform acceleration phase) maintains a slow acceleration, potentially insufficient to sustain further filament eruption. Conversely, the impulsive phase, synonymous with the eruption phase, accelerates the filament to significantly higher velocities. In fact, it is not uncommon for the impulsive increase in velocity to correlate well with the impulsive increase in SXR flux (Zhang et al., 2004). However, in certain events like this one, the impulsive increase in velocity or height precedes the impulsive increase in SXR flux by several minutes. In such cases, we believe that instability is more likely to trigger the eruption than reconnection. Consequently, we posit that torus instability, associated with the impulsive phase, serves as the primary triggering mechanism. Thus, the second aspect pertains to the role of magnetic reconnection. Based on the observational analysis, we believe the initial reconnection (related to the small bright patch observed south of the east footpoint of the bright arcade) plays a crucial role in initiating filament ascent and ultimately triggering instability, akin to the scenario outlined by Cheng et al. (2023). However, regarding the second reconnection, namely, the flare, delineating its specific contribution is challenging. Unlike active region filaments, quiescent filaments can erupt successfully without discernible reconnection signatures, as observed in the datasets of McCauley et al. (2015) and Zou et al. (2019b). Upon examining the

database of McCauley et al. (2015), we find that among quiescent filaments and polar crown filaments accompanied by flares (75 identified events), only 10% fail to produce CMEs. In contrast, approximately 36% of identified quiescent filaments and polar crown filaments do not result in CMEs. This leads us to infer that the flare or reconnection during the rapid rise phase likely contributes positively to CME formation, possibly through mechanisms such as the second reconnection in the tether-cutting model (Moore et al., 2001), which cut off the constraining field above, or via reconnection in the BASIC model (Jiang et al., 2021), which furnishes an upward tension force.

The third aspect pertains to how the torus instability is triggered. In the extrapolation presented earlier, the results indicate that the magnetic field lines we traced exhibit low twist, while torus instability typically correlates with magnetic flux ropes (MFRs) characterized by higher twist. Here, we propose two potential explanations. First, as mentioned in Section 3, it is plausible that an MFR is embedded within the magnetic lines depicted in Figure 5, although it may be undetectable due to the limitations of extrapolation in weak magnetic fields. Secondly, if the extrapolation is accurate, the MFR could form after the initial reconnection between the sheared arcades involved in the filament, thereby meeting the conditions for triggering torus instability. The formation of magnetic flux ropes through this type of reconnection has been achieved in the simulations of Jiang et al. (2021) and Bian et al. (2022). Thus, in either scenario, the establishment of an MFR is conceivable. However, this raises the question: why is the filament that is already under the torus unstable before the instability is actually triggered? In the case of the second inference, it is conceivable that the gradual process of reconnection requires time to form the MFR. Regarding the first inference, we propose that the observed drainage at both footpoints plays a key role. Simulations conducted by Fan (2018) and Zhang et al. (2021) suggest that the mass contained within the filament significantly influences the equilibrium of MFRs. Thus, we think the drainage would attenuate gravity and activate the instability.

In conclusion, we present a comprehensive scenario elucidating the evolution of the filament eruption process and the GOES flux curve. This narrative outlines the collaborative action of two mechanisms, namely, magnetic reconnection and torus instability, throughout the entire process of a filament eruption within a weak active region. Filaments characterized by weak magnetic fields seldom erupt through reconnection processes (Zou et al., 2019b). In our study, we confirm that the triggering mechanism of this eruptive filament is the torus instability. There should be two reconnections similar to the scenario described by Moore et al. (2001). The first reconnection is very gentle but forces the filament upward and triggers the torus instability. The second reconnection, corresponding to the flare, may contribute positively to the formation of the CME. This result contradicts the findings of Zou et al. (2019b). Therefore, we believe that a more detailed analysis is needed to confirm whether those filaments can be triggered by reconnection for filaments within the relatively weaker magnetic environment, where it can be difficult to distinguish the contribution of reconnection or instability.

Data availability statement

The raw data supporting the conclusions of this article will be made available by the authors, without undue reservation.

Author contributions

PZ: conceptualization, investigation, writing—original draft, writing—review and editing. CJ: funding acquisition, methodology, software, writing—review and editing. XB: methodology, writing—review and editing. JW: funding acquisition, writing—review and editing.

Funding

The author(s) declare that financial support was received for the research, authorship, and/or publication of this article. This work is supported by the National Natural Science Foundation of China (NSFC 12003005, 42174200), the Shenzhen Key Laboratory Launching Project (No. ZDSYS20210702140800001), and the Guangdong Basic and Applied Basic Research Foundation (2023B1515040021). Data from observations are courtesy of NASA SDO science teams.

References

- Antiochos, S. K., DeVore, C. R., and Klimchuk, J. A. (1999). A model for solar coronal mass ejections. *ApJ* 510, 485–493. doi:10.1086/306563
- Aulanier, G., Török, T., Démoulin, P., and DeLuca, E. E. (2010). *ApJ* 708, 314–333. doi:10.1088/0004-637x/708/1/314
- Bian, X., Jiang, C., Feng, X., Zuo, P., Wang, Y., and Wang, X. (2022). Numerical simulation of a fundamental mechanism of solar eruption with a range of magnetic flux distributions. *A&A* 658, A174. doi:10.1051/0004-6361/202141996
- Bobra, M. G., Sun, X., Hoeksema, J. T., Turmon, M., Liu, Y., Hayashi, K., et al. (2014). The helioseismic and magnetic imager (HMI) vector magnetic field pipeline: SHARPs – space-weather HMI active region patches. *SoPh* 289, 3549–3578. doi:10.1007/s11207-014-0529-3
- Carmichael, H. (1964). *A process for flares*. Washington, DC: NASA Special Publication.
- Chamberlin, P. C., Woods, T. N., Eparvier, F. G., and Jones, A. R. (2009). in *Society of photo-optical instrumentation engineers (SPIE) conference series. Solar physics and Space weather instrumentation*. Editors S. Fineschi, and J. A. Fennelly, III.743802
- Chen, P. F., Harra, L. K., and Fang, C. (2014). *APJ* 784, 50. doi:10.1088/0004-637x/784/1/50
- Chen, P. F., and Shibata, K. (2000). An emerging flux trigger mechanism for coronal mass ejections. *APJ* 545, 524–531. doi:10.1086/317803
- Cheng, X., Xing, C., Aulanier, G., Solanki, S. K., Peter, H., and Ding, M. D. (2023). Deciphering the slow-rise precursor of a major coronal mass ejection. *APJL* 954, L47. doi:10.3847/2041-8213/acf3e4
- Cheng, X., Zhang, J., Ding, M. D., and Poonvises, W. (2010). *APJ* 712, 752–760. doi:10.1088/0004-637x/712/1/752
- Démoulin, P. (2006). Extending the concept of separatrices to QSLs for magnetic reconnection. *Adv. Space Res.* 37, 1269–1282. doi:10.1016/j.asr.2005.03.085
- Duan, A., Jiang, C., Guo, Y., Feng, X., and Cui, J. (2022) *A&A*, 659, A25.
- Duan, A., Jiang, C., Zou, P., Feng, X., and Cui, J. (2021). Structure and evolution of an inter-active region large-scale magnetic flux rope. *APJ* 906, 45. doi:10.3847/1538-4357/abc701
- Fan, Y. (2018). MHD simulation of prominence eruption. *APJ* 862, 54. doi:10.3847/1538-4357/aacce
- Filippov, B. P., and Den, O. G. (2000). Prominence height and vertical gradient in magnetic field. *Astron. Lett.* 26, 322. doi:10.1134/1.20397
- Gary, G. A., and Hagyard, M. J. (1990). Transformation of vector magnetograms and the problems associated with the effects of perspective and the azimuthal ambiguity. *SoPh* 126, 21. doi:10.1007/BF00158295
- Hirayama, T. (1974). Theoretical model of flares and prominences: I: evaporating flare model. *SoPh* 34, 323–338. doi:10.1007/bf00153671
- Jenkins, J. M., Hopwood, M., Démoulin, P., Valori, G., Aulanier, G., Long, D. M., et al. (2019). Modeling the effect of mass-draining on prominence eruptions. *APJ* 873, 49. doi:10.3847/1538-4357/ab037a
- Jiang, C., Duan, A., Feng, X., Zou, P., Zuo, P., and Wang, Y. (2019). Reconstruction of a highly twisted magnetic flux rope for an inter-active-region X-class solar flare. *Front. Astronomy Space Sci.* 6, 63. doi:10.3389/fspas.2019.00063
- Jiang, C., and Feng, X. (2013). Extrapolation of the solar coronal magnetic field from *sdo/hmi* magnetogram by a *cese-mhd-nlfff* code. *APJ* 769, 144. doi:10.1088/0004-637x/769/2/144
- Jiang, C., Feng, X., Liu, R., Yan, X., Hu, Q., Moore, R. L., et al. (2021). A fundamental mechanism of solar eruption initiation. *Nat. Astron.* 5, 1126–1138. doi:10.1038/s41550-021-01414-z
- Jiang, C., Wu, S. T., Feng, X., and Hu, Q. (2014). Nonlinear force-free field extrapolation of a coronal magnetic flux rope supporting a large-scale filament from photospheric vector magnetogram. *Astrophysical J. Lett.* doi:10.1088/2041-8205/786/2/L16
- Jing, J., Liu, C., Lee, J., Wang, S., Wiegmann, T., Xu, Y., et al. (2014). Evolution of a magnetic flux rope and its overlying arcade based on nonlinear force-free field extrapolations. *APJL* 784, L13. doi:10.1088/2041-8205/784/1/L13
- Kliem, B., and Török, T. (2006). Torus instability. *PhRvL* 96, 255002. doi:10.1103/physrevlett.96.255002
- Kopp, R. A., and Pneuman, G. W. (1976). Magnetic reconnection in the corona and the loop prominence phenomenon. *SoPh* 50, 85. doi:10.1007/bf00206193
- Lemen, J. R., Title, A. M., Akin, D. J., Boerner, P., Chou, C., Drake, J. F., et al. (2012). The atmospheric imaging assembly (AIA) on the solar dynamics observatory (SDO). *SoPh* 275, 17. doi:10.1007/s11207-011-9776-8
- Lynch, B. J., Antiochos, S. K., MacNeice, P. J., Zurbuchen, T. H., and Fisk, L. A. (2004). Observable properties of the breakout model for coronal mass ejections. *APJ* 617, 589–599. doi:10.1086/424564
- Martin, S. F., Marquette, W. H., and Bilimoria, R. (1992). “Astronomical society of the pacific conference series,” *The solar cycle*. Editor K. L. Harvey, 53.

Conflict of interest

The authors declare that the research was conducted in the absence of any commercial or financial relationships that could be construed as a potential conflict of interest.

Publisher's note

All claims expressed in this article are solely those of the authors and do not necessarily represent those of their affiliated organizations, or those of the publisher, the editors and the reviewers. Any product that may be evaluated in this article, or claim that may be made by its manufacturer, is not guaranteed or endorsed by the publisher.

Supplementary material

The Supplementary Material for this article can be found online at: <https://www.frontiersin.org/articles/10.3389/fspas.2024.1369362/full#supplementary-material>

- McCauley, P. I., Su, Y. N., Schanche, N., Evans, K. E., Su, C., McKillop, S., et al. (2015). Prominence and filament eruptions observed by the solar dynamics observatory: statistical properties, kinematics, and online catalog. *SoPh* 290, 1703–1740. doi:10.1007/s11207-015-0699-7
- Metcalfe, T. R. (1994). *Soph* 155, 235–242. doi:10.1007/bf00680593
- Mierla, M., Seaton, D. B., Berghmans, D., Chifu, I., De Groof, A., Inhester, B., et al. (2013). Study of a prominence eruption using PROBA2/SWAP and STEREO/EUVI data. *SoPh* 286, 241–253. doi:10.1007/s11207-012-9965-0
- Moore, R. L., Sterling, A. C., Hudson, H. S., and Lemen, J. R. (2001). Onset of the magnetic explosion in solar flares and coronal mass ejections. *APJ* 552, 833–848. doi:10.1086/320559
- Peng, Z., Chaowei, J., Juntao, W., and Xinkai, B. (2022). Mechanism of the failed eruption of an intermediate solar filament. *APJ* 928, 160. doi:10.3847/1538-4357/ac581f
- Sakurai, T. (1976). Magnetohydrodynamic interpretation of the motion of prominences. *PASJ* 28, 177.
- Scherrer, P. H., Schou, J., Bush, R. I., Kosovichev, A. G., Bogart, R. S., Hoeksema, J. T., et al. (2012). The helioseismic and magnetic imager (HMI) investigation for the solar dynamics observatory (SDO). *SoPh* 275, 207–227. doi:10.1007/s11207-011-9834-2
- Schou, J., Scherrer, P. H., Bush, R. I., Wachter, R., Couvidat, S., Rabello-Soares, M. C., et al. (2012). Design and ground calibration of the helioseismic and magnetic imager (HMI) instrument on the solar dynamics observatory (SDO). *SoPh* 275, 229–259. doi:10.1007/s11207-011-9842-2
- Seaton, D. B., Hughes, J. M., Tadikonda, S. K., Caspi, A., DeForest, C. E., Krimchansky, A., et al. (2021). The Sun's dynamic extended corona observed in extreme ultraviolet. *Nat. Astron.* 5, 1029–1035. doi:10.1038/s41550-021-01427-8
- Srivastava, A. K., Mishra, S. K., and Jelínek, P. (2021). The prominence driven forced reconnection in the solar corona and associated plasma dynamics. *APJ* 920, 18. doi:10.3847/1538-4357/ac1519
- Sturrock, P. A. (1966). Model of the high-energy phase of solar flares. *nature* 211, 695–697. doi:10.1038/211695a0
- Titov, V. S., Hornig, G., and Démoulin, P. (2002). Theory of magnetic connectivity in the solar corona. *J. Geophys. Res. Space Phys.* 107, 1164. doi:10.1029/2001ja000278
- Török, T., and Kliem, B. (2005). Confined and ejective eruptions of kink-unstable flux ropes. *Astrophysical J.* doi:10.1086/462412
- Török, T., Kliem, B., and Titov, V. S. (2004). Ideal kink instability of a magnetic loop equilibrium. *A&A* 413, L27. doi:10.1051/0004-6361:20031691
- van Ballegoijen, A. A., and Martens, P. C. H. (1989). Formation and eruption of solar prominences. *APJ* 343, 971. doi:10.1086/167766
- Yashiro, S., Gopalswamy, N., Akiyama, S., Michalek, G., and Howard, R. A. (2005). Visibility of coronal mass ejections as a function of flare location and intensity. *J. Geophys. Res. Space Phys.* 110, A12S05. doi:10.1029/2005ja011151
- Zhang, J., Dere, K. P., Howard, R. A., and Vourlidas, A. (2004). A study of the kinematic evolution of coronal mass ejections. *APJ* 604, 420–432. doi:10.1086/381725
- Zhang, Q., Liu, R., Wang, Y., Li, X., and Lyu, S. (2021). Confined and eruptive catastrophes of solar magnetic flux ropes caused by mass loading and unloading. *APJ* 921, 172. doi:10.3847/1538-4357/ac1fef
- Zou, P., Jiang, C., Feng, X., Zuo, P., Wang, Y., and Wei, F. (2019a). A two-step magnetic reconnection in a confined X-class flare in solar active region 12673. *APJ* 870, 97. doi:10.3847/1538-4357/aaf3b7
- Zou, P., Jiang, C., Wei, F., Zuo, P., and Wang, Y. (2019b). A statistical study of solar filament eruptions that form high-speed coronal mass ejections. *APJ* 884, 157. doi:10.3847/1538-4357/ab4355